energies

Article

Eddy Current Braking Force Analysis of a Water-Cooled Ironless Linear Permanent Magnet Synchronous Motor

Mengyao Wang, Lu Zhang *, Kai Yang, Junjie Xu and Chunyu Du

Department of Electrical Engineering and Automation, Harbin Institute of Technology, Harbin 150080, China; wangmy@stu.hit.edu.cn (M.W.)
* Correspondence: zhanglu24@hit.edu.cn

Abstract: The ironless linear permanent magnet synchronous motor (ILPMSM) is highly compact, easy to control, and exhibits minimal thrust fluctuations, making it an ideal choice for direct loading applications requiring precise positioning accuracy in linear motor test rigs. To address the issue of temperature rise resulting from increased primary winding current and to simultaneously enhance thrust density while minimizing thrust fluctuations, this paper introduces a bilateral-type ILPMSM with a cooling water jacket integrated between the dual-layer windings of the primary movers. The primary winding of the motor adopts a dual-layer coreless structure where the upper and lower windings are closely spaced and cooled by a non-conductive metal cooling water jacket, while the dual-sided secondary employs a Halbach permanent magnet array. The motor's overall braking force is a combination of the electromagnetic braking force generated by the energized windings and the eddy current braking force induced on the cooling water jacket. This paper specifically focuses on the analysis of the eddy current braking force. Initially, the motor's geometry and working principle are presented. Subsequently, the equivalent magnetization intensity method is employed to determine the no-load air gap magnetic density resulting from the Halbach array. An analytical model is then developed to derive expressions for the eddy current density and braking force induced in the water-cooling jacket. The accuracy of the analytical method is validated through finite element analysis. Then, a comparative analysis of the braking forces in two primary cooling structures, namely the inter-cooled type and the two-side cooled type ILPMSM, is conducted. Moreover, the characteristics of the eddy current braking force are thoroughly examined concerning motor size parameters and operating conditions. This paper provides a solid theoretical foundation for the subsequent optimization design of the proposed motor.

Keywords: eddy current braking force; ironless linear permanent magnet motor; cooling water jacket; parameter effect analyze

Citation: Wang, M.; Zhang, L.; Yang, K.; Xu, J.; Du, C. Eddy Current Braking Force Analysis of a Water-Cooled Ironless Linear Permanent Magnet Synchronous Motor. *Energies* **2023**, *16*, 5826. https://doi.org/10.3390/en16155826

Academic Editor: Salvatore Musumeci

Received: 30 June 2023
Revised: 1 August 2023
Accepted: 4 August 2023
Published: 6 August 2023

1. Introduction

Linear motor performance testing covers a broad range of aspects, with the motor loading test serving as a key component [1]. Traditional testing platforms often encounter problems such as inadequate precision, slow response, and an inability to maintain continuous loading. Nevertheless, the trend is shifting toward the direct loading technique of linear motors, increasingly preferred for its rapid response, contactless transmission, and high accuracy [2,3]. The introduction of Ironless Linear Permanent Magnet Synchronous Motors (ILPMSMs) has further increased the loading precision of testing platforms. Although these motors have reduced thrust density due to the absence of iron cores in their primary coils, their non-cogging and low thrust fluctuation attributes make them ideal for high-precision, non-positioning systems [4].

Increasing the thrust density of ILPMSMs requires amplifying the current in the primary winding. This elevation in current leads to a greater demand for copper, which in turn results in a notable temperature rise. As the coreless structure inherently lacks good thermal conductivity, the need for supplemental cooling devices becomes crucial.

Compared with their iron-core counterparts, Linear Permanent Magnet Synchronous Motors (LPMSMs) demonstrate superior thrust stability and excel at low-speed performance, free from tooth slot effects and thrust fluctuations due to core discontinuity. However, these motors typically display lower thrust levels and thrust density [5]. In recent years, the focus of LPMSM design optimization has been on reducing thrust fluctuation and enhancing thrust density. Research has primarily concentrated on two interconnected aspects: electromagnetic structure and cooling structure design, which are both dependent on the relationship between the electromagnetic, fluid, and temperature fields. Considering the cooling structure's substantial impact on the motor's electromagnetic performance, this study emphasizes the analysis of the electromagnetic field within the cooling structure.

Analytical methods for temperature rise and cooling structure design in coreless motors fall into two categories: the lumped parameter equivalent thermal circuit method [6,7] and numerical calculation methods based on partial differential equations [8,9]. Various cooling strategies for high-power linear or planar motors have been proposed by domestic and international research institutions. These strategies include direct or indirect cooling utilizing water-cooled plates, or water pipes installed on the primary or secondary side [10–15]. Notably, Nikon Corporation has patented a direct cooling scheme for linear and planar motors used in high-precision microelectronic equipment, such as lithographic machines. This scheme involves a fully enclosed cooling bracket and direct cooling to dissipate heat generated by the winding [11]. Sun and Liu utilized a cooling plate and water tank structure installed on the upper surface of the primary side of a flat-type permanent magnet linear synchronous motor [12,13]. However, this approach requires a specialized water tank that is cumbersome and inconvenient to install during primary winding encapsulation. Liu and Chen designed a water-cooling system for a moving-coil permanent magnet synchronous planar motor, where cooling water jackets were installed on the upper surface of the encapsulated coils [14,15]. Liu [14] compared and analyzed the cooling effects of N-shaped and U-shaped water channel structures, ultimately selecting the U-shaped cooling water channel and conducting optimization design. Chen proposed three new flow channel structures: series-parallel flow channel structure, double series flow channel structure, and spiral flow channel structure, based on an analysis of the heat dissipation performance of traditional series and parallel water channels [15]. The spiral flow channel structure, which provides better comprehensive performance and temperature uniformity, was applied in the actual prototype. Pan developed a multi-objective model based on genetic algorithms and designed an iron-coreless DC motor with a bilateral water-cooling machine structure for ultra-precision position servo systems [16,17]. The table-type water-cooled plate consists of multiple C-shaped copper foil heat transfer rings distributed in sections, which are installed on the upper and lower surfaces of the primary winding. This structure effectively mitigates the temperature rise on the upper and lower surfaces of the motor's primary side.

Past research has mainly centered on the design and optimization of cooling structures, employing thermal circuit methods or finite element methodologies for analyzing and computing temperature fields. Concurrently, the interplay between temperature and electromagnetic fields is deemed negligible. In essence, while improving cooling structure design, the modifications in electromagnetic thrust density and fluctuation rate are not usually factored into the constraints and optimization goals. Existing studies on water cooling systems for linear motors outline three distinctive categories of cooling devices: cooling water jackets installed in the primary structure for heat dissipation through circulating water; cooling water channels embedded in the primary core or windings, also utilizing circulating water for heat dissipation; and cooling water tanks that are installed around the primary side to augment the heat transfer area via forced cooling methods. All these cooling devices have demonstrated effective cooling results and their application depends on specific use cases. Despite the burgeoning research on water cooling devices, the effect of these devices on motor thrust and thrust fluctuation has not been a central theme, highlighting ample opportunity for further exploration. In high-precision applications, the damping effect of eddy currents from cooling devices on electromagnetic thrust (which can reach up to 10% in extreme conditions [18]) warrants a quantitative analysis. This is essential to understanding the influence of cooling devices on the electromagnetic structure.

This paper aims to design a water-cooled, iron-coreless permanent magnet linear motor, ILPMSM, that meets high thrust, rapid response, and high precision requirements, and to analyze the eddy current braking force in the cooling jacket. The main contributions of this paper are twofold: Firstly, the proposal of a dynamic primary-side bilateral iron-coreless linear permanent magnet synchronous motor with a cooling device. This motor functions as the load motor for a linear motor test platform and features high thrust density and low thrust fluctuation. Secondly, the analysis of eddy current braking forces in the cooling water jacket and the quantitative analysis of the structural parameters of the cooling device's impact on motor thrust. This provides a theoretical foundation for the subsequent optimization of the motor's electromagnetic structure and cooling structure.

The rest of this paper is organized as follows: Section 2 establishes a two-dimensional layered analytical model of a motor with a cooling water jacket and derives expressions for the induced eddy current density and eddy current braking force within the water jacket. Section 3 uses the FEA for model verification, and further compares the eddy current braking forces of two primary structures: the intermediate cooling type and the bilateral cooling type. Section 4 focuses on analyzing the influence of motor size and other parameters on braking force density and thrust fluctuation. Finally, Section 5 concludes this paper with a comprehensive summary.

2. Eddy Current Analysis in the Cooling Water Jacket of the Proposed ILPMSM

2.1. Geometry

This paper presents a novel ILPMSM with a water-cooling system, as shown in Figure 1. Figure 1a illustrates the 3D assembly of the Ironless Permanent Magnet Synchronous Motor (ILPMSM), while Figure 1b provides a schematic representation of its electromagnetic geometry. The linear motor comprises a primary mover with an ironless coil and a double-sided secondary stator with a U-shaped yoke. The primary mover features a dual-layer three-phase hollow winding, adopting a short-pitch concentrated winding configuration. The cooling water jacket is positioned between the upper and lower layers of the primary winding, facilitating forced water cooling through the circulating cooling water supply. The secondary part consists of a dual-sided Halbach magnet array and a U-shaped flux-conducting yoke plate.

The electromagnetic part and the working principle of the proposed ILPMSM share similarities with the conventional double-sided LPMSM. However, the novel contributions of this study lie in introducing the alloy cooling system and analyzing the resulting eddy current braking force problem. Specifically, to achieve high thrust density, low thrust fluctuation, and a wide range of braking forces, an ironless core primary structure, and an aluminum alloy cooling water jacket to directly cool the primary winding are adopted. The cooling water jacket employs a parallel double water path topology to enhance heat dissipation [19,20]. Figure 2a illustrates this configuration, while Figure 2b shows the arrangement of cooling water channels relative to the coils. Each coil side has two cooling water channels symmetrically placed, and the two coil sides of the same coil are arranged as one inlet and one return, ensuring the even distribution of the motor primary's temperature rise. The centrally positioned cooling water jacket is fully encapsulated with epoxy resin, serving as both a cooling water channel and structural support for the coil.

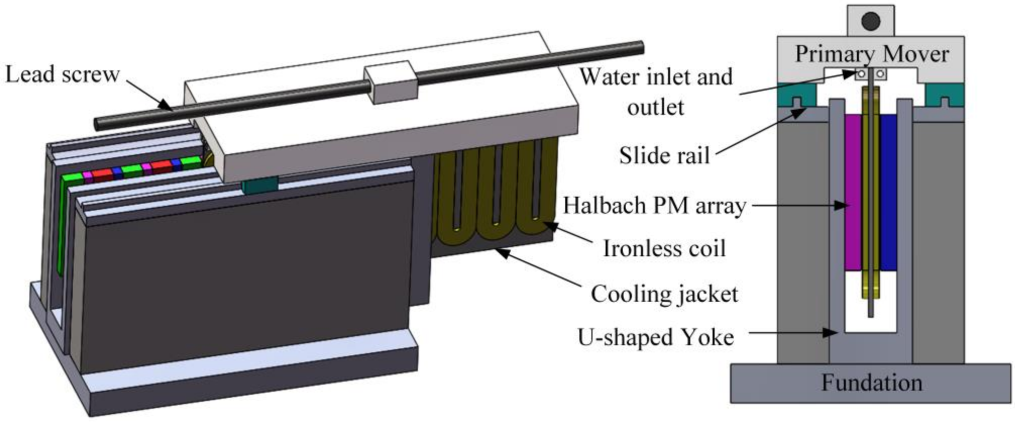

(**a**)

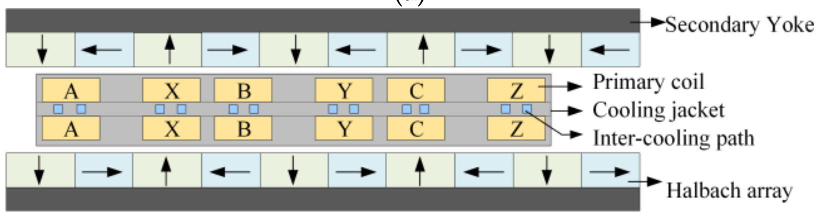

(**b**)

Figure 1. The geometry of the proposed ILPMSM: (**a**) 3D assembly drawing; (**b**) 2D electromagnetic structure.

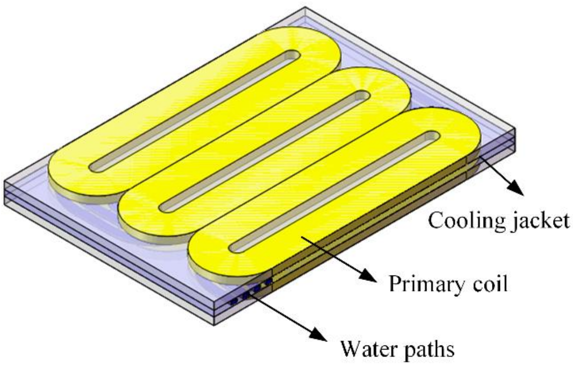

(**a**)

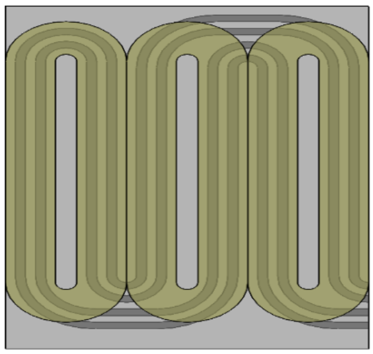

(**b**)

Figure 2. The geometry of the Primary: (**a**) partial cross-section; (**b**) cooling water paths.

2.2. Analytical Model of the Eddy Current

In this section, we adopt the approach of theoretical analysis to illustrate the eddy current distribution in the cooling water jacket. The cooling water jacket utilized in this study is constructed from impermeable metal material, resulting in the induction of eddy currents within the jacket during primary motion. These eddy currents interact with the magnetic field, generating an eddy-braking force. The magnitude of this braking force is analyzed using an analytical approach. Initially, the vortex density within the cooling water jacket is determined, focusing on the primary structure of the two side windings with middle cooling. The side effects of the cooling water jacket are neglected, and a two-dimensional parallel plane field assumption is made for the magnetic field. The analytical model depicting this configuration is presented in Figure 3.

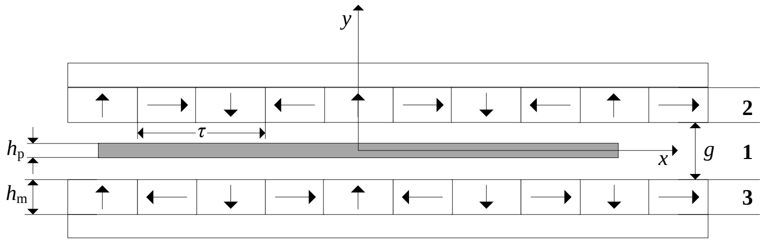

Figure 3. The analytical model of ILPMSM.

To simplify the analysis process, several assumptions are made [21,22]:

1. The model extends indefinitely in the x and z directions.
2. The magnetic permeability inside the cooling water jacket aligns with vacuum permeability, and the electrical conductivity is consistent.
3. The magnetic field around the cooling water jacket is assumed to be the no-load air-gap magnetic field, without the consideration of eddy current demagnetization effects.
4. The presence of eddy currents is only contemplated in the z-direction.
5. The effects of slotting inside the cooling water jacket are overlooked.
6. Only the primary wave component of the air-gap magnetic density is considered.

By employing the equivalent magnetization intensity method [21], the Halbach permanent magnet array can be equated to the magnetization intensity function. The expression of the magnetization intensity function along the x-direction is as follows:

$$M_{\mathrm{x}} = \sum_{n=1}^{\infty} \frac{4B_{\mathrm{r}}}{(2n-1)\pi\mu_0} \cos\frac{(2n-1)\pi\alpha_p}{2} \sin\frac{(2n-1)\pi x}{\tau} \tag{1}$$

where B_{r} is the residual magnetization strength of the permanent magnet, μ_0 denotes the magnetic permeability of the air, τ represents the pole pitch of the permanent magnet array, and α_p represents the major PM pole pitch ratio.

In the air gap region 1, the vector magnetic potential satisfies Laplace's equation. In the permanent magnet regions 2 and 3, the vector magnetic potential satisfies Poisson's equation. The complete set of equations for the vector magnetic potential within the entire region is established as follows:

$$\begin{cases} \frac{\partial^2 A_{z1}}{\partial x^2} + \frac{\partial^2 A_{z1}}{\partial y^2} = 0 \\ \frac{\partial^2 A_{z2}}{\partial x^2} + \frac{\partial^2 A_{z2}}{\partial y^2} = -\mu_0 \frac{\partial M_{\mathrm{x}}}{\partial x} \\ \frac{\partial^2 A_{z3}}{\partial x^2} + \frac{\partial^2 A_{z3}}{\partial y^2} = \mu_0 \frac{\partial M_{\mathrm{x}}}{\partial x} \end{cases} \tag{2}$$

Equation (2) satisfies the following boundary conditions:

$$\begin{cases} B_{\mathrm{y1}}\Big|_{y=\frac{1}{2}g} = B_{\mathrm{y2}}\Big|_{y=\frac{1}{2}g} & B_{\mathrm{y1}}\Big|_{y=-\frac{1}{2}g} = B_{\mathrm{y2}}\Big|_{y=-\frac{1}{2}g} \\ H_{\mathrm{y2}}\Big|_{y=\frac{1}{2}g} - H_{\mathrm{y1}}\Big|_{y=\frac{1}{2}g} = M_{\mathrm{x}} & H_{\mathrm{y2}}\Big|_{y=-\frac{1}{2}g} - H_{\mathrm{y1}}\Big|_{y=-\frac{1}{2}g} = -M_{\mathrm{x}} \\ H_{\mathrm{y2}}\Big|_{y=\frac{1}{2}g+h_{\mathrm{m}}} = M_{\mathrm{x}} & H_{\mathrm{y2}}\Big|_{y=-\frac{1}{2}g-h_{\mathrm{m}}} = -M_{\mathrm{x}} \end{cases} \tag{3}$$

$$B_{\mathrm{y}} = -\frac{\partial A_{\mathrm{z}}}{\partial x} \tag{4}$$

The general solution Equation (2) can be obtained by applying the separation of variables method. By substituting the boundary conditions, the expression for the vector magnetic potential can be derived. Then, using the electromagnetic field Equation (4), the expression for the radial component of the air gap magnetic density can be obtained. In the subsequent calculations, only the radial air gap magnetic density of the air gap region is considered. Therefore, this paper does not provide the expressions for the air gap magnetic density in each region. Only the expressions for the fundamental components of the air gap magnetic density are presented as follows:

$$B_{y1} = B_{ym}\cosh\left(\frac{\pi}{\tau}y\right)\cos\left(\frac{\pi}{\tau}x\right) \tag{5}$$

$$B_{ym} = -\frac{\pi}{\tau}\left\{\begin{array}{l} \frac{K}{\sinh\left[\frac{\pi}{\tau}\left(\frac{g}{2}+h_m\right)\right]} - \frac{\left[K\cosh\left(\frac{\pi}{\tau}\frac{g}{2}\right)+T\sinh\left(\frac{\pi}{\tau}\frac{g}{2}\right)\right]\cosh\left[\frac{\pi}{\tau}\left(\frac{g}{2}+h_m\right)\right]}{\sinh\left[\frac{\pi}{\tau}\left(\frac{g}{2}+h_m\right)\right]} \\ +K\sinh\left(\frac{\pi}{\tau}\frac{g}{2}\right) + T\cosh\left(\frac{\pi}{\tau}\frac{g}{2}\right) \end{array}\right\} \tag{6}$$

where g is the air gap length, h_m corresponds to the thickness of the permanent magnet, and h_p is the thickness of the cooling water jacket. In Equation (6), the parameters K and T are defined as follows:

$$K = \frac{4\tau B_r}{\pi^2}\cos\left(\frac{\pi\alpha_p}{2}\right) \tag{7}$$

$$T = -\frac{4\tau B_r}{\pi^2}\sin\left(\frac{\pi\alpha_p}{2}\right) \tag{8}$$

Equation (5) portrays the magnetic density of the air gap around the cooling water jacket, presuming the demagnetization effect of the cooling water jacket's eddy current is overlooked. Following this, we separately calculate the vector magnetic potential A_z within the cooling water jacket, which helps us derive the expression for eddy current density. The magnetic vector potential A_z inside the cooling water jacket is governed by the second-order differential complex partial differential equation (PDE) in the Cartesian coordinates.

$$\frac{\partial^2 A_z}{\partial x^2} + \frac{\partial^2 A_z}{\partial y^2} = j\omega\mu\sigma A_z \tag{9}$$

$$\frac{\partial^2 A_z}{\partial x^2} + \frac{\partial^2 A_z}{\partial y^2} = \mu\sigma\frac{\partial A_z}{\partial t} \tag{10}$$

where A_z stands for the vector magnetic potential within the cooling water jacket. The angular frequency is represented by ω, while μ denotes the magnetic permeability and σ the electrical conductivity of the cooling water jacket.

At the moment t = 0, Equation (10) satisfies the following boundary conditions.

$$\left\{\begin{array}{l} B_y\Big|_{y=\frac{1}{2}h_p} = B_{ym}\cosh\left(\frac{\pi}{\tau}\frac{1}{2}h_p\right)\cos\left(\frac{\pi}{\tau}x\right) \\ B_y\Big|_{y=-\frac{1}{2}h_p} = B_{ym}\cosh\left(-\frac{\pi}{\tau}\frac{1}{2}h_p\right)\cos\left(\frac{\pi}{\tau}x\right) \end{array}\right. \tag{11}$$

The generalized form of Equation (10) can be obtained using the separation of variables method as follows:

$$A_z = C_1\left[e^{-\alpha y}\sin\left(\omega t - \frac{\pi}{\tau}x - \beta y + \theta_1\right) + e^{\alpha y}\sin\left(\omega t - \frac{\pi}{\tau}x + \beta y + \theta_1\right)\right] \tag{12}$$

$$\left\{\alpha = \gamma\cos\varphi, \beta = \gamma\sin\varphi,\ \gamma^2 = \sqrt{(\pi/\tau)^4 + (\omega\mu\sigma)^2},\ \varphi = \frac{1}{2}\arctan\left(\frac{\omega\mu\sigma}{(\pi/\tau)^2}\right)\right\} \tag{13}$$

The partial derivative of Equation (12) can be found as follows:

$$\theta_1 = -\arctan\left(\tanh\left(\frac{\alpha h_p}{2}\right)\tan\left(\frac{\beta h_p}{2}\right)\right),\ C_1 = \frac{B_{ym}\cosh\left(\frac{\pi h_p}{2\tau}\right)}{\frac{\pi}{\tau}\sqrt{2\cosh(\alpha h_p) + 2\cos(\beta h_p)}} \tag{14}$$

After obtaining the vector magnetic potential A_z, according to the electromagnetic field equation and Ampere's law, the z-component of the induced eddy current density J_z can be obtained as follows:

$$\left\{ H_x = \frac{1}{\mu}\frac{\partial A_z}{\partial y},\ H_y = -\frac{1}{\mu}\frac{\partial A_z}{\partial x},\ J_z = \frac{\partial H_y}{\partial x} - \frac{\partial H_x}{\partial y} \right\} \tag{15}$$

$$J_z = -\frac{2C_1\alpha\beta}{\mu}\left[e^{-\alpha y}\cos\left(\omega t - \frac{\pi}{\tau}x - \beta y + \theta_1\right) + e^{\alpha y}\cos\left(\omega t - \frac{\pi}{\tau}x + \beta y + \theta_1\right)\right] \tag{16}$$

2.3. Analysis of Eddy Current Braking Force

In this study, the LPMSM utilized a Halbach structure for the secondary component, a hollow winding for the primary component, and a significant air gap. Due to these design characteristics, the armature reaction can be disregarded, and the cooling water jacket is assumed to experience an unloaded air gap magnetic density. The analytical model for the eddy current braking force is depicted in Figure 4, which represents the moment $t = 0$. In the figure, "v" denotes the synchronous speed of the motor, "L_p" signifies the length of the cooling water jacket, "h_{w1}" represents the thickness of the upper coil, and "h_{w2}" corresponds to the thickness of the lower coil.

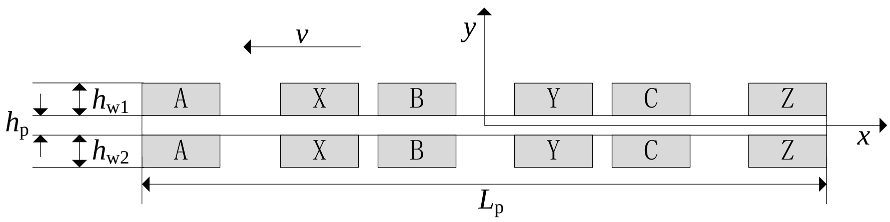

Figure 4. The analytical model of braking force.

Based on the vector magnetic potential derived for the cooling water jacket in Section 2.2, the expression for the radial component of the magnetic density within the cooling water jacket can be obtained as follows:

$$B_y = -\frac{\partial A_z}{\partial x} \tag{17}$$

$$B_y = C_1 m_1\left[e^{-\alpha y}\cos\left(\omega t - \frac{\pi}{\tau}x - \beta y + \theta_1\right) + e^{\alpha y}\cos\left(\omega t - \frac{\pi}{\tau}x + \beta y + \theta_1\right)\right] \tag{18}$$

At any given moment, the differential form of the tangential eddy current braking force is as

$$dF_{x2} = B_y J_z l_w dxdy \tag{19}$$

where l_w is the transverse width of the cooling water jacket, and J_z represents the z-component of the current density induced in the cooling water jacket.

Starting from the moment $t = 0$, the expression for the eddy current braking force F_{x2} on the motor is as follows:

$$\begin{aligned} F_{x2} &= \iint dF_{x2}dxdy \\ &= \frac{2C_1{}^2\pi\alpha\beta l_w}{\mu_0\tau}\int_{-\frac{L_p}{2}-vt}^{\frac{L_p}{2}-vt}\int_{-\frac{h_p}{2}}^{\frac{h_p}{2}}\left[e^{-\alpha y}\cos\left(-\frac{\pi}{\tau}x - \beta y + \theta_1\right) + e^{\alpha y}\cos\left(-\frac{\pi}{\tau}x + \beta y + \theta_1\right)\right]^2 dxdy \\ &= \frac{2C_1{}^2\pi l_w}{\mu_0\tau}\left[\beta\sinh(\alpha h_p) + \alpha\sin(\beta h_p)\right]L_p + \frac{C_1{}^2C_2\alpha\beta l_w}{\mu_0}\sin\left(\frac{\pi}{\tau}L_p\right)\sin(2\omega t + \theta_2) \end{aligned} \tag{20}$$

$$\begin{cases} C_2 = \sqrt{C_3^2 + 4h_p^2 + 2C_3\sin(\theta_3 - \varphi)} \\ \theta_2 = 2\theta_1 + \arctan\frac{C_3\cos(\theta_3-\varphi)}{C_3\cos(\theta_3-\varphi)-2h_p} \\ C_3 = \frac{\sqrt{2\cosh(2\alpha h_p)-2\cos(2\beta h_p)}}{\gamma} \\ \theta_3 = \arctan\left(\coth(\alpha h_p)\tan(\beta h_p)\right) \end{cases} \tag{21}$$

Equation (20) represents the analytical expression for the vortex braking force F_{x2}. By examining Equation (20), it becomes evident that the vortex braking force comprises two components: a constant component and a fluctuating component. Furthermore, the magnitude and fluctuation of the eddy current braking force are influenced by the dimensions of the cooling water jacket and the operational speed of the motor.

3. Finite Element Validation and Comparison Analysis

3.1. Finite Element Verification of Intermediate Water-Cooled ILPMSM

An FEA-simulation model is developed to analyze an ILPMSM with an intermediate water-cooled jacket. Figure 5a illustrates the simulation model and Figure 5b a sectional view of the topology, respectively. The 2D FEA-simulation model involves selecting specific materials for different components: steel_1010 for the secondary yoke plate, NdFeB38 with a magnetization direction of 90 degrees for the Halbach permanent magnet alloy, copper for the coils, and either stainless steel or aluminum alloy for the cooling water jacket. Since the primary coil is in motion, a movement domain is set in the simulation to account for its movement. The primary operates at a rated speed of 3 m/s during the simulation. The key parameters for the FEA-simulation model are in Table 1.

To depict the overall structure of the cooling water jacket, we provide a physical representation of the prototype. The integrated cooling structure of the ILPMSM prototype's primary cooling water jacket is presented in Figure 6. Given the slim thickness of the cooling water jacket, direct drilling was impractical for its fabrication. As a result, the cooling water jacket was divided into two parts, left and right, for individual machining, and the completed jacket was then assembled through adhesion.

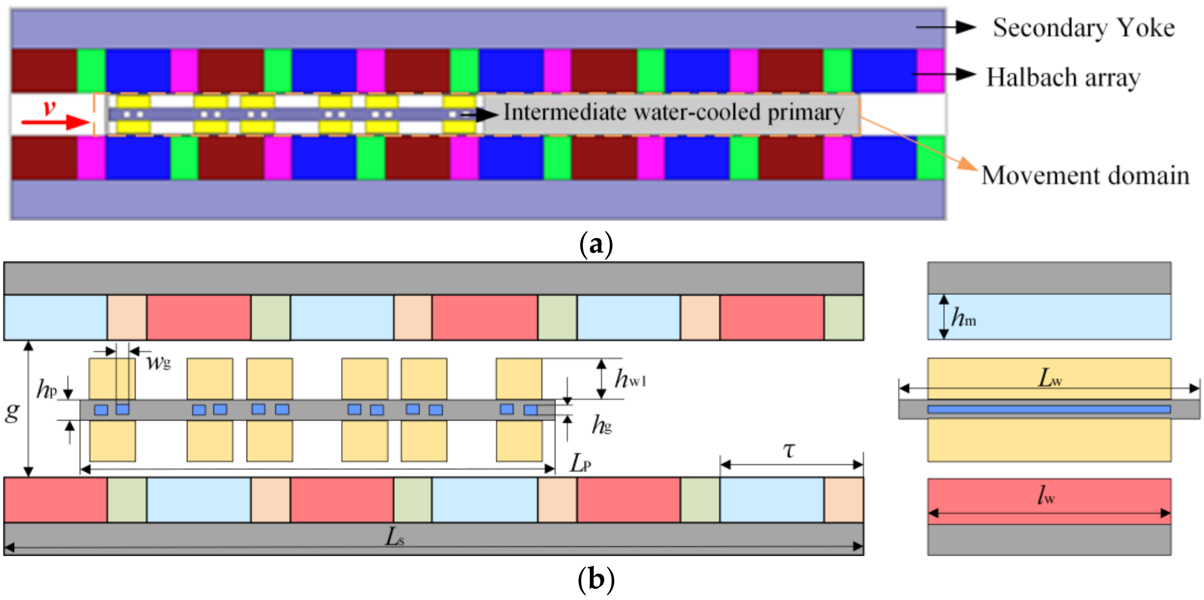

Figure 5. The FEA-simulation model of the ILPMSM with an intermediate water-cooled jacket: (**a**) 2D FEA-simulation model; (**b**) sectional views of the topology.

Table 1. Parameters of the studied ILPMSM.

Symbol	Quantity	Value	Symbol	Quantity	Value
h_m	PM thickness	10.5 mm	α_p	Major PM pole pitch ratio	0.68
l_m	PM horizontal length	80 mm	h_{w1}	Upper coil thickness	3.5 mm
I_f	Rated phase current	10.8 A	N	Turns of armature winding	304
g	Air-gap length	10.5 mm	B_{ym}	Air gap magnetic density amplitude	0.8 T
τ	Pole pitch	24 mm	w_g	Water path width	6 mm
l_w	Cooling jacket transverse width	80 mm	h_g	Water path thickness	3 mm
h_p	Cooling jacket thickness	2 mm	L_w	Primary transverse width	141 mm
L_p	Cooling jacket length	100 mm	Ls	Secondary length	432 mm

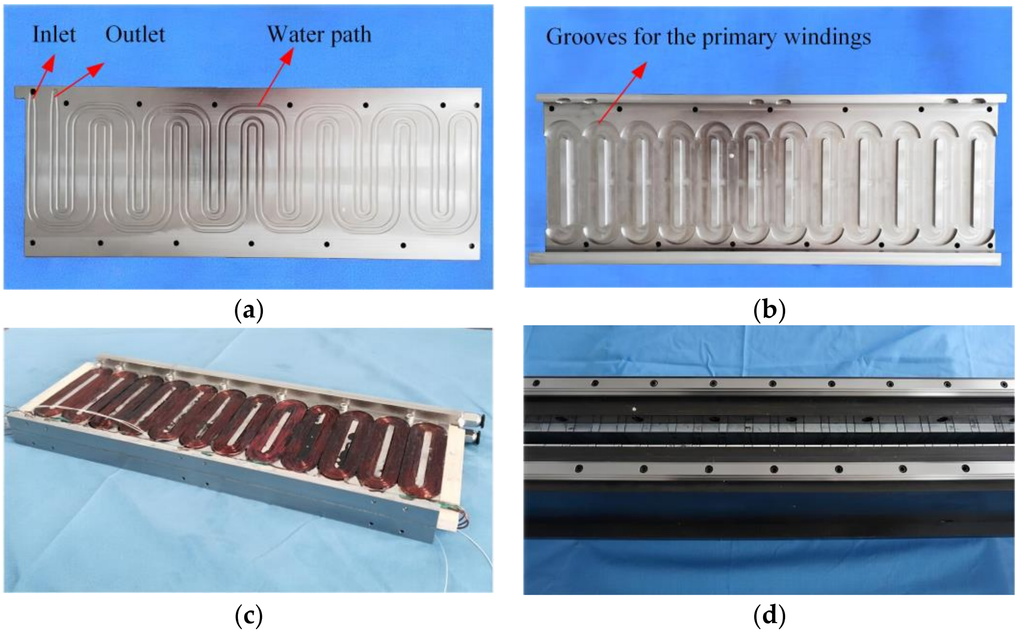

Figure 6. Prototype photos for the ILPMSM with an intermediate water-cooled jacket: (**a**) the water path side of the cooling water jacket; (**b**) the primary coil side of the cooling water jacket; (**c**) the primary prototype before potting; (**d**) the secondary prototype.

Figure 6a shows the water path side of the cooling water jacket. A cooling water path is carved on one side of the jacket, allowing the cooling water to enter through an inlet, circulate along the channel, and then exit through an outlet. On the opposite side of the cooling water jacket, as shown in Figure 6b, a recess is carved to accommodate the coil. Figure 6c,d are photos of the primary prototype before potting and the secondary prototype, respectively.

Upon bonding the left and right cooling water jackets, the corresponding coil is situated in the recess. The entire assembly of the cooling water jacket and the coil is then sealed with epoxy, completing the motor's primary processing.

It is important to note, as discernable from the physical illustration, the direct contact between the coils and the cooling water jacket facilitates efficient heat transfer. The prototype's cooling water jacket is composed of stainless steel, a material known for its high thermal conductivity. This enables the majority of the heat within the jacket to be dissipated via water circulation, effectively reducing the motor's primary temperature rise.

The eddy current braking force comparison between the FEA and the analytical model is shown in Figure 7 when the linear motor operates at a constant speed of 2.4 m/s. The two methods yield similar vortex braking force curves, with an average value of 13.76 N obtained from the analytical method and 13.45 N obtained from the finite element method. The difference between the two values is 0.31 N, which accounts for 2.25% of the amplitude of the vortex braking force obtained from the simulation. The slightly higher values obtained from the analytical method can be attributed to the neglect of magnetic leakage, longitudinal edge-end effects, and demagnetization effects in the analytical approach. Furthermore, the fluctuation of the eddy current braking force in the graph follows a sinusoidal pattern, which is consistent with Equation (20). From the data in the figure, it can be calculated that the amplitude of the fluctuating component is 0.78 N for the analytical method and 0.91 N for the finite element method. The lower amplitude of the fluctuating component in the analytical method is attributed to the neglect of harmonic effects.

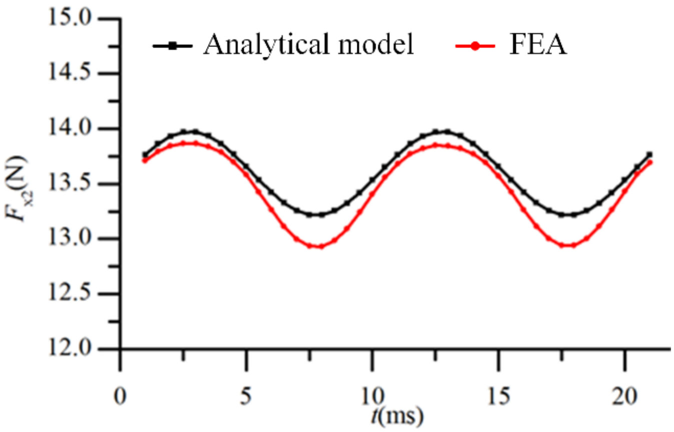

Figure 7. FEA and analytical comparison of eddy current braking.

Additionally, the effect of slotting in the cooling water jacket was not considered in the analytical method in Section 2.2, namely a solid plate. The slotting effect refers to the presence of double-loop water paths inside the cooling water jacket, as shown in Figures 5b and 6a. These water paths create a non-solid structure for the cooling water jacket, resembling multiple transverse slots within. To evaluate this effect, the FEA was used with the parameters and dimensions of the motor in Table 1, considering the symmetrical arrangement of six cooling water slots.

The comparison of the eddy current braking force before and after slotting is shown in Figure 8. As observed in Figure 8, the mean value of the eddy current braking force decreases and becomes less smooth after slotting, while the amplitude of the fluctuation slightly increases. However, the overall trend is consistent with the curve obtained through the analytical method that neglects to slot, thus confirming the validity of the aforementioned assumptions.

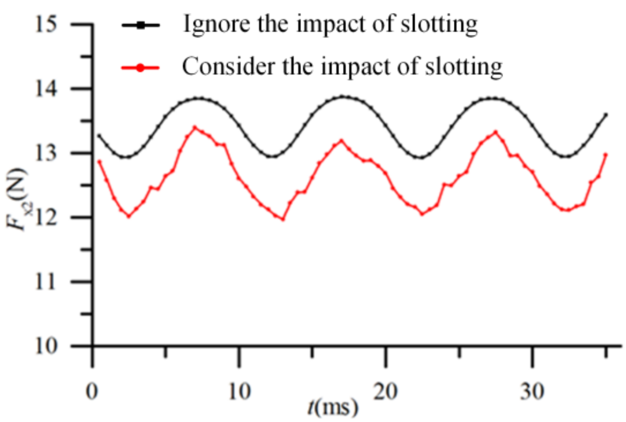

Figure 8. The influence of cooling water slotting on eddy current braking force by FEA.

3.2. Braking Force Comparison of Two Primary Structure ILPMSM

The primary structure of the motor consists of a two-sided cooling intermediate winding, where the cooling water jacket is installed on both sides of the coil for heat dissipation. Figure 9 illustrates the finite element model and primary structure of a motor with water cooling on both sides.

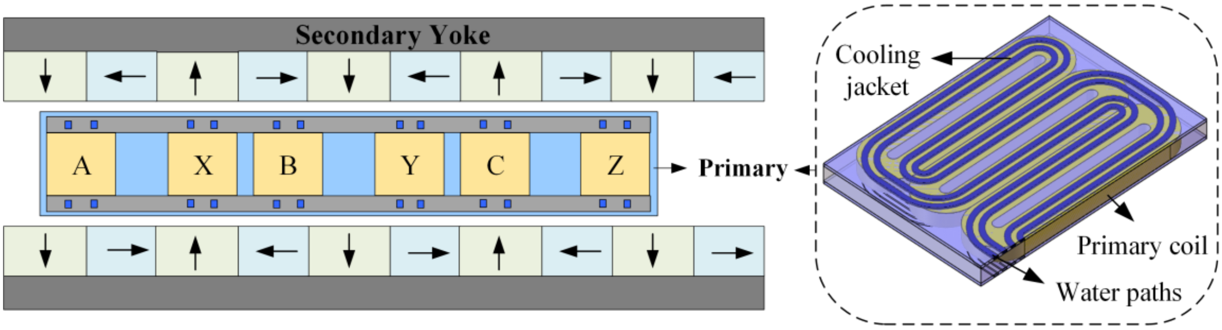

Figure 9. The FEA model of the ILPMSM with two-side water-cooling jacket.

By applying the method described in Section 2, the expression for the eddy current braking force can also be derived for the motor with cooling on both sides of the winding. The analytical results are then verified using the FEA method, as shown in Figure 10a. To compare the eddy current braking forces of the two primary structures, certain parameters such as the air-gap length and the pole spacing of the ILPMSM were kept consistent with those in Table 1. Additionally, the total thickness of the primary winding and the total thickness of the cooling water jacket were the same for both structures. Under these equivalence conditions, the eddy current braking forces of the two cooling structures were compared, as shown in Figure 10b.

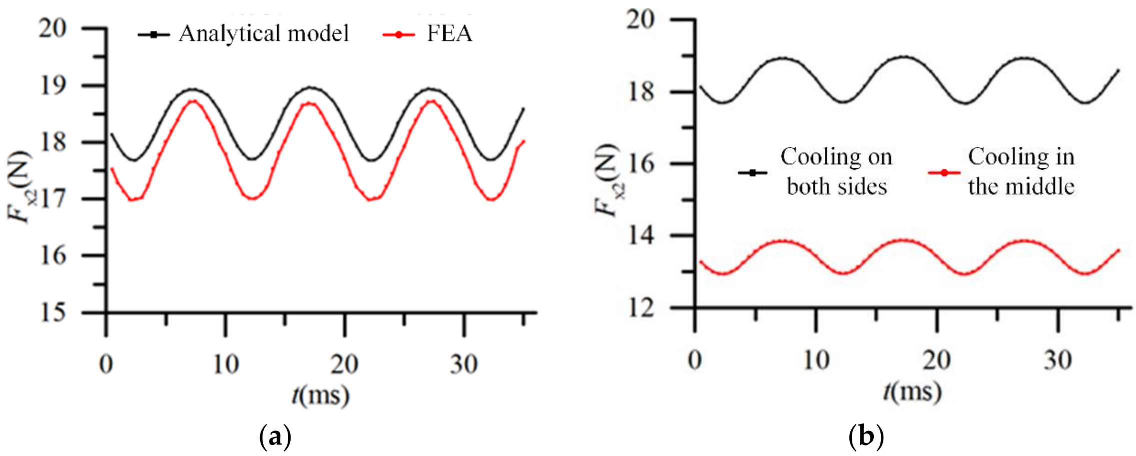

Figure 10. Comparison of eddy current braking force between analytical and FEA: (**a**) two-side water cooling ILPMSM; (**b**) comparison between two cooling structures of ILPMSM.

As observed in Figure 10a, the eddy current braking force curves obtained using both methods closely match. The analytical method yields a mean value of 18.32 N, while the finite element method yields a mean value of 17.78 N, resulting in a difference of 0.54 N, which accounts for 3.03% of the mean value obtained from the simulation. As evidenced in Figure 10b, the eddy current braking force induced in the middle cooling is marginally less than that generated in the two-sided cooling, at a ratio of 0.76. Concurrently, the fluctuation of the braking force in the middle cooling is somewhat smaller than in the two-sided cooling, with a ratio of 0.88. The eddy current braking force is larger in the two-sided cooling because the cooling water jacket's spatial position is nearer to the permanent magnet. Consequently, the magnetic field strength is more significant across the entire cooling water jacket area, leading to a greater eddy current braking force throughout this region.

It can be concluded that the primary structure with cooling on both sides can generate a slightly higher braking force density due to the stronger magnetic field strength. However, it should be noted that the eddy current braking force only constitutes a small portion of the total braking force. The primary structure with cooling on both sides also reduces the electromagnetic braking force generated by energizing the winding due to the magnetic isolation effect, which needs to be taken into consideration. Additionally, the cooling effect is another aspect of comparison between the two configurations, apart from the eddy current braking force. Therefore, the final primary solution should be determined by considering all factors comprehensively.

4. Characteristics Analysis of the ILPMSM on Eddy Current Braking Force

In the design of the loading motor, the total braking force density and braking force fluctuation are the key considerations. While there are existing methods to study electromagnetic braking force, this paper specifically focuses on the investigation of eddy current braking force density and fluctuation. As mentioned previously, according to Equation (20), the eddy current braking force can be divided into two components: a constant component and a fluctuating component. The amplitude of the constant component of the eddy current braking force is denoted as F_{x21}, and the constant eddy current braking force density is defined as $\boldsymbol{f_{x1}}$. The amplitude of the fluctuating component of the eddy current braking force is defined as $\boldsymbol{F_{x22}}$, and the fluctuating eddy current braking force density is denoted as f_{x2}, given by the following expression:

$$f_{x1} = \frac{F_{x21}}{h_p L_p l_w} \tag{22}$$

$$f_{x2} = \frac{F_{x22}}{h_p L_p l_w} \tag{23}$$

f_{x1} is the magnitude of the braking force and f_{x2} reflects the fluctuation of the braking force. h_p, L_p, and l_w are the cooling water jacket thickness, cooling water jacket length, and cooling water jacket horizontal width, respectively. Next, the parameter effect on f_{x1} and f_{x2} is studied for the ILPMSM of the intercooler structure.

4.1. Effect of Cooling Water Jacket Thickness on Eddy Current Braking Force

By keeping the other parameters of the motor constant and varying only the value of the cooling water jacket thickness (h_p), we can observe the variation patterns of f_{x1} and f_{x2} concerning h_p. These patterns are illustrated in Figure 11a,b, respectively.

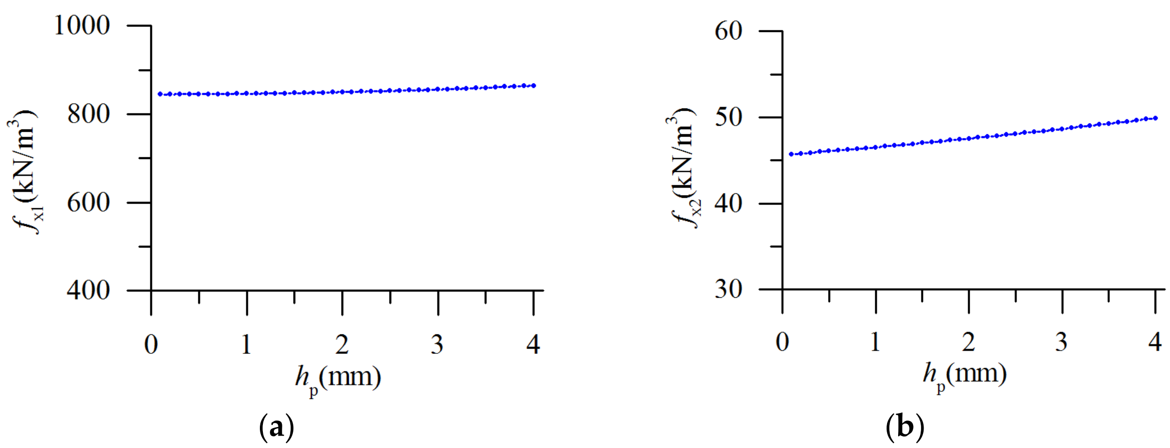

Figure 11. The curve of cooling water jacket thickness h_p with braking force magnitude f_{x1} and fluctuation f_{x2}: (**a**) the curve of f_{x1} with h_p; (**b**) the curve of f_{x2} with h_p.

In Figure 11a, it can be observed that f_{x1} increases slowly as h_p increases. However, since the range of variation for hp is limited, the range of variation for f_{x1} is not significant. Therefore, it can be assumed that the eddy current braking force density remains relatively constant with increasing h_p. On the other hand, Figure 11b shows that f_{x2} increases linearly and monotonically with increasing h_p. This suggests that the thickness of the cooling water jacket should be reduced to minimize the fluctuation of the eddy current braking force. A thinner cooling water jacket can help to stabilize the braking force.

However, it is important to consider that the total braking power of the motor primarily comes from electromagnetic braking power, while the eddy current braking power only contributes a small portion to the total. Increasing the thickness of the cooling water jacket can enhance the cooling capacity of the primary motor, allowing for higher current values in the primary winding, which in turn increases the electromagnetic braking power and the total braking power. Therefore, when selecting the thickness of the cooling water jacket, all these factors should be taken into consideration.

4.2. Effect of L_p/τ on Eddy Current Braking Force

From Equation (20), it can be seen that the fluctuating component of the vortex braking force is related to the value of the cooling jacket length/pole pitch (L_p/τ). Therefore, the structural parameter L_p/τ is chosen, keeping the other parameters constant, and the variation laws of f_{x1} and f_{x2} with L_p/τ are shown in Figure 12a and Figure 12b, respectively.

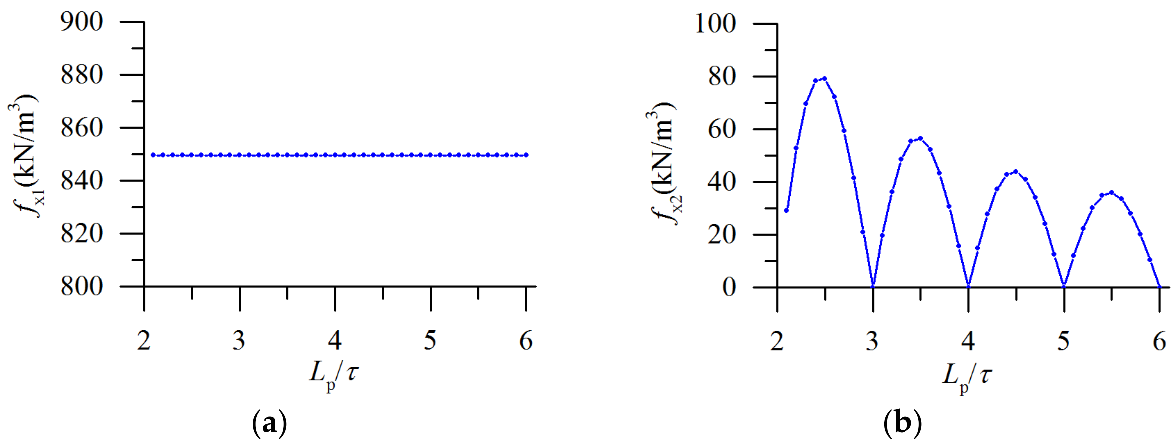

Figure 12. The curve of L_p/τ with braking force magnitude f_{x1} and fluctuation f_{x2}: (**a**) the curve of f_{x1} with L_p/τ; (**b**) the curve of f_{x2} with L_p/τ.

As can be seen from Figure 12a, the variation of f_{x1} concerning L_p/τ remains constant. As can be seen in Figure 12b, f_{x2} decays sinusoidally as L_p/τ becomes larger and reaches a minimum when the length of the cooling water jacket is equal to an integer multiple of the pole pitch. It should be noted here that since the analytical method ignores the effect of harmonics, a solution with a f_{x2} of zero is obtained, whereas, in the finite element simulation, f_{x2} tends to be consistent with L_p/τ but does not decrease to zero. Based on the above analysis, the motor should be designed so that the length of the cooling water jacket is equal to an integer multiple of the pole pitch.

4.3. Effect of Pole Pitch and Major PM Pole Pitch Ratio on Eddy Current Braking Force

The permanent magnet array determines the size of the air gap magnetic density and the waveform, which in turn affects the eddy current braking force, and it is necessary to analyze the effect of the secondary primary dimensions on the eddy current braking force.

In Figure 13a, it is evident that the eddy current braking force density, f_{x1}, increases rapidly as the pole pitch τ becomes larger. After reaching a pole pitch of 28 mm, the eddy current braking force density stabilizes. This indicates that increasing the pole pitch can significantly enhance the eddy current braking force density.

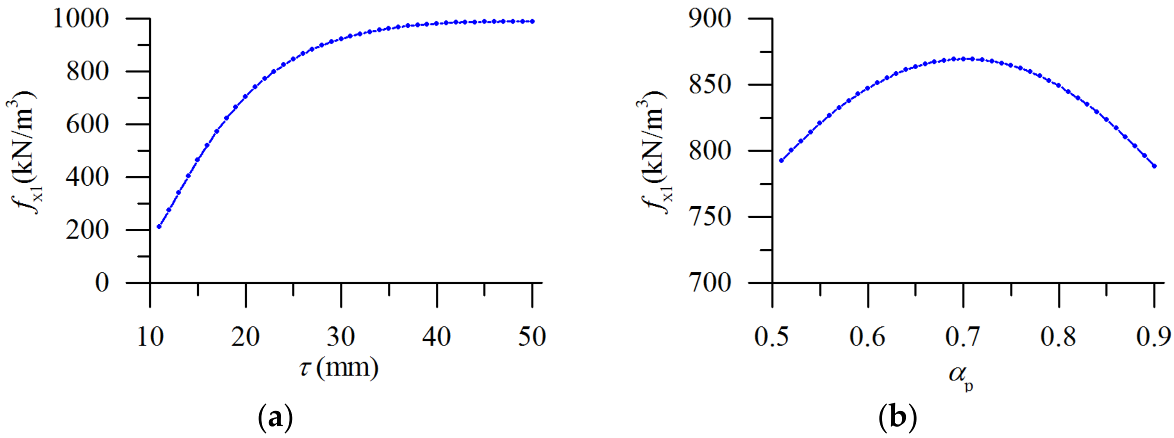

Figure 13. The curve of pole pitch τ and major PM pole pitch ratio α_p with braking force magnitude f_{x1}: (**a**) the curve of f_{x1} with τ; (**b**) the curve of f_{x1} with α_p.

Figure 13b demonstrates that f_{x1} exhibits a nonlinear relationship with the main permanent magnet pole pitch ratio, α_p. As a reminder, the ratio of the permanent magnet width to the pole pitch is often referred to as the permanent magnet width ratio (pole pitch ratio). Initially, as α_p increases, f_{x1} increases. However, after reaching a peak value around α_p = 0.7, f_{x1} starts to decrease. This suggests that there is an optimal value for αp that maximizes the vortex braking force density.

By appropriately adjusting these parameters, it is possible to optimize the eddy current braking force density, thereby improving the performance of the motor.

4.4. Effect of Other Parameters on Eddy Current Braking Force

The analysis of the vortex braking force concerning various factors is crucial once the structural parameters of the motor have been determined. The magnitude of the vortex braking force is directly influenced by the motor's operating speed and the material chosen for the cooling water jacket. Therefore, it is essential to investigate the impact of speed variations on the vortex braking force. In this study, three different speeds were selected for analysis, as depicted in Figure 14, to examine the magnitude of the vortex braking force, denoted as F_{x2}, at different speeds.

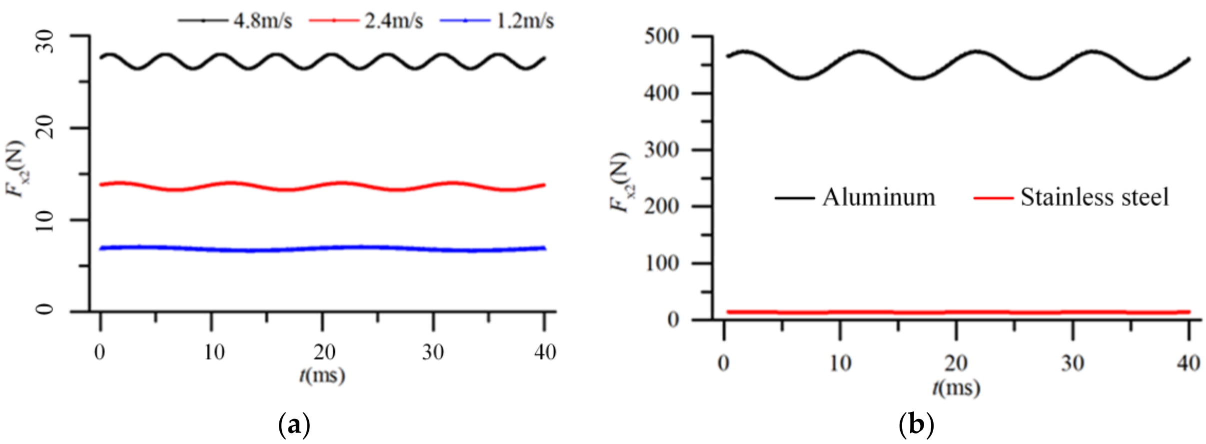

Figure 14. The effect of velocity and materials on eddy current braking force: (**a**) working speed; (**b**) material of cooling water jacket.

The results presented in Figure 14a indicate that, as the motor speed increases, both the average value and the fluctuation amplitude of the eddy current braking force increase. Additionally, the frequency of the force fluctuation is directly proportional to the motor speed. Thus, when designing the motor, a careful analysis of the eddy current braking force should be performed, taking into consideration the motor's speed.

Furthermore, the choice of material for the cooling water jacket also affects the eddy current braking force due to the different conductivities of various materials. Therefore, it is necessary to investigate the relationship between the eddy current braking force and the chosen material. Figure 14b illustrates the magnitude of the eddy current braking force, F_{x2}, when using aluminum and stainless steel for the cooling water jacket.

Considering the superior thermal conductivity of aluminum compared with stainless steel, selecting aluminum as the material for the cooling water jacket yields better cooling efficiency. As depicted in Figure 14b, when aluminum is used as the cooling water jacket material, the vortex braking force exhibits a significant increase, along with a notable increase in the force's fluctuation amplitude, reaching 47.4 N. Consequently, the total braking force experiences larger fluctuations. However, if the experimental requirements necessitate higher running speeds and lower loading forces, the choice of aluminum alloy as the cooling water jacket material may not provide a smooth loading force, thus failing to meet the experimental requirements. In such cases, considering both the thermal conductivity of the cooling water jacket and the motor's application, it is advisable to opt for stainless steel as the material for the cooling water jacket.

In summary, once the structural parameters of the motor are determined, the magnitude and fluctuation of the eddy current braking force are primarily influenced by the motor's operating speed and the material chosen for the cooling water jacket. The careful consideration of these parameters is crucial to meet the specific requirements of the motor's operation and experimental needs.

5. Conclusions

In this paper, an ILPMSM with a water-cooling jacket is proposed for loading applications. The analysis focuses on the eddy current braking force generated on the cooling water jacket, leading to the following key conclusions:

1. The analytical model utilizing the equivalent magnetization intensity method accurately calculates the no-load air gap magnetic density. Analytical expressions for the vortex density in the cooling water jacket and the vortex braking force are derived. Finite element simulations validate the accuracy of the analytical model.
2. A comparative analysis of the braking forces in two primary cooling structures, namely the inter-cooled type and the two-sided cooled type ILPMSM, reveals that the inter-cooled type ILPMSM exhibits smaller braking force fluctuations. On the other hand, the two-sided cooled ILPMSM demonstrates slightly higher braking force density.
3. The vortex braking force in the cooling water jacket is decomposed into a constant component and a fluctuating component. A detailed analysis is conducted to investigate the influence of motor structural parameters, movement speed, and the material of the cooling water jacket on these two components of the vortex braking force. The findings provide a theoretical foundation for subsequent motor designs.

In summary, this paper presents a comprehensive analysis of the eddy current braking force in an ILPMSM. The derived analytical expressions and the insights gained from the comparative analysis offer valuable guidance for the design of such motors in practical applications.

Author Contributions: Conceptualization, funding acquisition, supervision, verification, and writing—review and editing, L.Z.; methodology, formal analysis, and writing—original draft, M.W.; software and investigation, K.Y., J.X. and C.D. All authors have read and agreed to the published version of the manuscript.

Funding: This research was funded by the National Natural Science Foundation of China 52077042.

Data Availability Statement: Not applicable.

Conflicts of Interest: The authors declare no conflict of interest.

References

1. Wang, X.; Wang, Y.; Wu, T. The Review of Electromagnetic Field Modeling Methods for Permanent-Magnet Linear Motors. *Energies* **2022**, *15*, 3595.
2. Tang, X. Comparison of linear motor and ball screw drive-based applications. *Automot. Tech.* **2018**, *9*, 36–39.
3. Li, Y.; Zhou, H. A review of research on coreless permanent magnet synchronous linear motors for the precision servo. *Microelectromechanics* **2008**, *5*, 71–76.
4. Kim, S.I.; Hong, J.P.; Kim, Y.K.; Nam, H.; Cho, H.I. Optimal design of slotless-type PMLSM considering multiple responses by response surface methodology. *IEEE Trans. Magn.* **2006**, *42*, 1219–1222.
5. Kefalas, T.D.; Kladas, A.D. Thermal Investigation of Permanent-Magnet Synchronous Motor for Aerospace Applications. *IEEE Trans. Ind. Electron.* **2014**, *61*, 4404–4411.
6. Mellor, P.H.; Roberts, D.; Turner, D.R. Lumped parameter thermal model for electrical machines of TEFC design. *IEEE Proc. B Electr. Power Appl.* **1991**, *138*, 205–218.
7. Jang, C.; Kim, J.Y.; Kim, Y.J.; Kim, J.O. Heat Transfer Analysis and Simplified Thermal Resistance Modeling of Linear Motor Driven Stages for SMT Applications. *IEEE Trans. Common. Packag. Technol.* **2003**, *26*, 532–540. [CrossRef]
8. Pei, Z.; Zhao, J.; Song, J.; Zong, K.; He, Z.; Zhou, Y. Temperature field calculation and water-cooling structure design of coreless permanent magnet synchronous linear motor. *IEEE Trans. Ind. Electron.* **2021**, *68*, 1065–1076. [CrossRef]
9. Zhou, Q.; Huang, S.; Zhang, Q.; Chi, F.; Zhang, X.; Xie, G. Analysis of stator temperature field of an ultra-high precision planar motor with new cooling structure. *Proc. CSEE* **2012**, *32*, 134–139+5.
10. Kou, B.; Zhao, B.; Cao, H. High-Precision Slotless Permanent Magnet Motor. CN Patent 102,185,458B, 27 March 2013.
11. Gao, Y.; Liao, Y.; Wang, G.; Fu, X. Moving Coil Linear Motor. CN Patent 101,009,453, 1 August 2007.
12. Binnard, M.B.; Arai, Y.; Hazelton, A.J. System for Cooling Motor. U.S. Patent 0,232,145, 19 October 2006.
13. Zhang, L.; Kou, B.; Chen, Y. Analysis and calculation of eddy current braking force for an ironless linear synchronous motor with a cooling system. In Proceedings of the 2016 19th International Conference on Electrical Machines and Systems (ICEMS), Chiba, Japan, 13–16 November 2016.
14. Liu, Z. Heat Dissipation and Experimental Research of Permanent Magnet Synchronous Planar Motor. Ph.D. Dissertation, University of Electronic Science and Technology, Chengdu, China, 2013.
15. Chen, X. Research on Water-Cooled Heat Dissipation System of Permanent Magnet Synchronous Planar Motor. Ph.D. Dissertation, University of Electronic Science and Technology, Chengdu, China, 2015.
16. Pan, D. Research on Accurate Modeling and Optimization of Coreless DC Linear Motor for the Ultra-Precise Positioning System. Ph.D. Dissertation, Harbin Institute of Technology, Harbin, China, 2013.
17. Li, L.; Pan, D.; Xiong, S.; Zhou, Y.; Tang, Y.; Chen, Q.; Guo, Q. The Cooling Structure of Ultra-Precision Linear Motor. CN Patent 102,882,314B, 12 December 2013.
18. Li, L.; Pan, D.; Huang, X. Analysis and optimization of ironless permanent-magnet linear motor for improving thrust. *IEEE Trans. Plasma Sci.* **2013**, *41*, 1188–1192. [CrossRef]
19. Wu, H.; Hsiao, Y.; Huang, H.; Tang, P.; Chen, S. A practical plate-fin heat sink model. *Appl. Therm. Eng.* **2011**, *31*, 984–992. [CrossRef]
20. Qu, W.; Mudawar, I. Experimental and numerical study of pressure drop and heat transfer in a single-phase micro-channel heat sink. *Int. J. Heat Mass Transf.* **2002**, *45*, 2549–2565. [CrossRef]
21. Jang, S.M.; Lee, S.H. Comparison of two types of PM linear synchronous servo and miniature motor with air-cored film coil. *IEEE Trans. Magn.* **2002**, *38*, 3264–3266. [CrossRef]
22. Mohammadpour, A.; Gandhi, A.; Parsa, L. Winding factor calculation for analysis of back EMF waveform in air-core permanent magnet linear synchronous motors. *IET Electr. Power Appl.* **2012**, *6*, 253–259. [CrossRef]